The Astrophysical Journal, 940:148 (11pp), 2022 December 1 https://doi.org/10.3847/1538-4357/ac9bf8

Compton-thick AGN in the NuSTAR Era. IX. A Joint NuSTAR and XMM-Newton Analysis of Four Local AGN

R. Silver[1], N. Torres-Albà[1], X. Zhao[1,2], S. Marchesi[1,3], A. Pizzetti[1], I. Cox[1], M. Ajello[1], G. Cusumano[4], V. La Parola[4], and A. Segreto[4]
[1] Department of Physics and Astronomy, Clemson University, Kinard Lab of Physics, Clemson, SC 29634, USA; rmsilve@clemson.edu
[2] Center for Astrophysics | Harvard & Smithsonian, 60 Garden Street, Cambridge, MA 02138, USA
[3] INAF—Osservatorio di Astrofisica e Scienza dello Spazio di Bologna, Via Piero Gobetti, 93/3, 40129, Bologna, Italy
[4] INAF—Istituto di Astrofisica Spaziale e Fisica Cosmica, Via Ugo la Malfa, 153, I-90146 Palermo PA, Italy
Received 2022 July 25; revised 2022 September 28; accepted 2022 October 17; published 2022 November 30

Abstract

We present the results of the broadband X-ray spectral analysis of simultaneous NuSTAR and XMM-Newton observations of four nearby Compton-thick active galactic nuclei (AGN) candidates selected from the Swift Burst Alert Telescope 150 month catalog. This work is part of a larger effort to identify and characterize all Compton-thick ($N_{\rm H} \geqslant 10^{24}\,{\rm cm}^{-2}$) AGN in the local universe ($z \leqslant 0.05$). We used three physically motivated models—`MYTorus`, `borus02`, and `UXClumpy`—to fit and characterize these sources. Of the four candidates analyzed, 2MASX J02051994-0233055 was found to be an unobscured ($N_{\rm H} < 10^{22}\,{\rm cm}^{-2}$) AGN, 2MASX J04075215-6116126 and IC 2227 to be Compton-thin ($10^{22}\,{\rm cm}^{-2} < N_{\rm H} < 10^{24}\,{\rm cm}^{-2}$) AGN, and one, ESO 362−8, was confirmed to be a Compton-thick AGN. Additionally, every source was found to have a statistically significant difference between their line-of-sight and average torus hydrogen column density, further supporting the idea that the obscuring material in AGN is inhomogeneous. Furthermore, half of the sources in our sample (2MASX J02051994-0233055 and 2MASX J04075215-6116126) exhibited significant luminosity variation in the last decade, suggesting that this might be a common feature of AGN.

Unified Astronomy Thesaurus concepts: Active galactic nuclei (16); X-ray active galactic nuclei (2035)

1. Introduction

Active galactic nuclei (AGN) are supermassive black holes (SMBHs) in the center of galaxies that accrete gas from their surrounding material. It is believed AGN are responsible for creating the majority of the cosmic X-ray background (CXB), the diffuse emission observed from 1 to 200−300 keV (e.g., Alexander et al. 2003; Gilli et al. 2007; Treister et al. 2009; Ueda et al. 2014; Brandt & Yang 2021). Particularly, a significant fraction (15%–20%; Gilli et al. 2007; Ananna et al. 2019) at the peak of the CXB (∼30 keV; Ajello et al. 2008) emanates from a population of AGN with line-of-sight obscuring column densities $N_{\rm H,l.o.s.} \geqslant 10^{24}\,{\rm cm}^{-2}$, known as Compton-thick AGN (CT-AGN). Moreover, population synthesis models, created to properly explain the origins of the CXB, predict CT-AGN comprise between 20% (Ueda et al. 2014) and 50% (Ananna et al. 2019) of all AGN. However, in the nearby universe ($z < 0.1$), CT-AGN represent only 5%−10% of the observed AGN (Comastri 2004; Della Ceca et al. 2008; Burlon et al. 2011; Ricci et al. 2015; Torres-Albà et al. 2021).

These sources are difficult to detect due to the significant obscuration of emission with energies ⩽10 keV (Gilli et al. 2007; Koss et al. 2016). Moreover, the majority of their emission comes from the so-called Compton hump at ∼20−40 keV. Therefore, an instrument that is sensitive in this energy range is necessary to study CT-AGN in the local universe. While the Swift Burst Alert Telescope (BAT) is capable of detecting these sources, it does not have the sensitivity required to accurately characterize CT-AGN (Barthelmy et al. 2005). Only the Nuclear Spectroscopic Telescope Array (NuSTAR; Harrison et al. 2013), with a sensitivity 2 orders of magnitude greater than Swift-BAT, can characterize the physical properties of these heavily obscured AGN (Baloković et al. 2014; Marchesi et al. 2017b; Ursini et al. 2018; Zhao et al. 2019a, 2019b; Baloković et al. 2021). However, the AGN spectrum at energies ⩾10 keV varies marginally with changing line-of-sight column density, whereas, soft X-rays (<10 keV) vary significantly (see, e.g., Gilli et al. 2007). For that reason, XMM-Newton, a soft X-ray instrument with the best effective area in 0.3–10 keV (∼10 times better than the Swift X-Ray Telescope and ∼2 times better than Chandra), is needed, in conjunction with NuSTAR, to perform a robust characterization of obscured AGN.

The Clemson-INAF Compton Thick AGN project[5] has been developed to find and characterize all obscured AGN in the local universe by targeting CT-AGN candidates from the 150 month BAT catalog (K. Imam et al. 2022, in preparation). Our first step is to select high-latitude ($|b| > 10°$), low-z ($z < 0.1$) Seyfert 2 (Sy2) galaxies or sources classified as normal galaxies (as the absence of broad lines implies the presence of obscuring material in our line of sight) that do not have a ROSAT counterpart (Voges et al. 1999) in the 0.1–2.4 keV band. Next, soft X-ray (Chandra) snapshots (∼10 ks) are obtained and fit alongside BAT data to obtain preliminary column density measurements to identify the best obscured-AGN candidates (see, e.g., Marchesi et al. 2017a, 2017b; Silver et al. 2022, hereafter, S22). The final step is to obtain simultaneous XMM-Newton and NuSTAR observations of these candidates to confirm their Compton-thick nature and to characterize the parameters of the torus, i.e., the obscuring dusty gas surrounding the SMBH.

[5] https://science.clemson.edu/ctagn/

Table 1
Summary of XMM-Newton and NuSTAR Observations

Source Name	Instrument	Sequence ObsID	Start Time (UTC)	End Time (UTC)	z	Exposure (ks)	Net Count Rate (10^{-2} counts s^{-1})
2MASX J02051994-0233055	XMM-Newton	0870850101	2020-07-04 21:25	2020-07-05 07:32	0.0283	36.4	5.65
	NuSTAR	60601026002	2020-07-04 21:36	2020-07-05 06:10		30.1	4.45
2MASX J04075215-6116126	XMM-Newton	0870850201	2021-02-22 15:23	2021-02-23 15:18	0.0214	86.1	0.82
	NuSTAR[a]	60601027002	2021-02-22 14:26	2021-02-23 01:44		40.7	...
	NuSTAR	60601036002	2021-02-27 20:01	2021-02-28 08:56		46.5	2.25
ESO 362-8	XMM-Newton	0890440101	2021-10-05 13:10	2021-10-05 23:44	0.0158	38.0	0.26
	NuSTAR	60701048002	2021-10-05 02:11	2021-10-05 15:40		48.5	1.41
IC 2227	XMM-Newton	0890440201	2022-03-27 23:57	2022-03-28 10:31	0.0323	38.0	0.64
	NuSTAR	60701049002	2022-03-28 05:46	2022-03-28 20:15		52.2	2.44

Notes. Average count rate (in counts per second), weighted by the exposure for XMM-Newton and NuSTAR, where observations from multiple instruments are combined. Count rates are computed in the 2−10 keV and 3−70 keV bands, respectively.
[a] This observation was not used in the analysis due to abnormally high background levels.

We have identified four nearby galaxies as obscured-AGN candidates, 2MASX J02051994-0233055 and 2MASX J04075215−6116126 from S22, and ESO 362−8 and IC 2227 from archival data. In this paper, we present the results of the NuSTAR-XMM-Newton analysis of these four sources. This work proceeds as follows: Section 2 lists the observations and data reduction of our four sources. Section 3 discusses the models used in analyzing the data and derived results. Section 4 compares these new results to the previous values found in S22, as well as reports the progress our team has made thus far in detecting CT-AGN in the local universe. All errors reported in this paper are at a 90% confidence level. Standard cosmological parameters are as follows: $H_0 = 70\,km\,s^{-1}\,Mpc^{-1}$, $q_0 = 0.0$, and $\Lambda = 0.73$.

2. Observation and Data Analysis

The four sources we analyze are selected from the BAT 150 month catalog,[6] a catalog of 1390 AGNs that Swift-BAT detected in the 15–150 keV band. Both 2MASX J02051994−0233055 and 2MASX J04075215−6116126 are listed as galaxies. Meanwhile, ESO 362−8 is an Sy2 galaxy and IC 2227 is an AGN.

2MASX J02051994−0233055 was originally selected as a potentially heavily obscured AGN in S22. 2MASX J04075215−6116126 was also studied in S22 and its selection is further discussed in Section 2.2.1. Subsequently, they were targeted by Chandra with 10 ks snapshots (proposal ID 19700430, PI: Marchesi). The Chandra data were fit with Swift-BAT to obtain a preliminary line-of-sight column density measurement for each source. 2MASX J02051994-0233055 had a best-fit $N_{H,l.o.s.} \sim 10^{25}\,cm^{-2}$ and 2MASX J04075215-6116126 had $N_{H,l.o.s.} \sim 2 \times 10^{23}\,cm^{-2}$. The low statistics of Chandra prevented us from confirming whether these sources were indeed CT-AGN and from characterizing properties of the torus. To do this, we obtained joint NuSTAR−XMM-Newton observations of each source (proposal ID 6220, PI: Ajello). ESO 362-8 and IC 2227 were selected as candidates following the procedure of S22, and existing archival data (XMM; Swift-XRT, respectively) were fit with BAT spectra, thus identifying them as CT-AGN candidates. Consequently, they were selected for joint NuSTAR−XMM-Newton observations as well (proposal ID 7219, PI: Silver). A summary of the observations is reported in Table 1.

[6] https://science.clemson.edu/ctagn/bat-150-month-catalog/

2.1. XMM-Newton Observations

All XMM-Newton observations were reduced using the Science Analysis System (Jansen et al. 2001) version 18.0.0. None of the observations were affected by flares. A 15″ circular region was used to extract the spectrum of each source. The background spectra were extracted using an annulus centered on the source with a 75″ inner radius and a 100″ outer radius. The image was visually inspected to ensure no contamination in the background from nearby sources. All three modules—MOS1, MOS2, and pn—are jointly fit in the modeling with their normalizations tied together, assuming marginal cross-calibration uncertainties.

2.2. NuSTAR Observations

NuSTAR observed all sources quasi-simultaneously with XMM-Newton, with the exception of 2MASX J04075215−6116126, as discussed below. The data are derived from both focal plane modules, FPMA and FPMB. The `nupipeline` version 0.4.8 was used to calibrate, clean, and screen the raw data files. The NuSTAR calibration database version 20200813 was used in this analysis. The `nuproducts` script was used to produce the redistribution matrix function, auxiliary response function, and light-curve files. For both modules, circular 50″ regions were used to extract the source spectra and an annulus with an inner radius 100″ and outer radius 150″ was used to extract the background spectra. The images were visually inspected to verify no nearby sources contaminated the background. The HEAsoft task `grppha` was used to group both the NuSTAR and XMM-Newton data with 25 counts per bin.

2.2.1. NuSTAR Observations of 2MASX J04075215-6116126

The first NuSTAR observation of 2MASX J04075215-6116126, which was interrupted due to a Target of Opportunity, was originally centered on ESO 118 IG 004 NED01 as the target due to the misassociation of the BAT source and no significant X-ray emission was found at the center of the observation. We then discovered that 2MASX J04075215-6116126 was the true BAT counterpart by analyzing the Chandra observation of this field in detail as presented in S22. Therefore, the following NuSTAR observation (ID: 60601036002) was centered on 2MASX J04075215-6116126. Additionally, we note that the first NuSTAR observation (60601027002) was taken near the South Atlantic Anomaly and thus has higher background levels than

Table 2
Power-law Fit of 2MASX J02051994-0233055 NuSTAR-XMM-Newton

χ^2/dof	Γ	$N_{\rm H,los}$	norm 10^{-2}	$c_{\rm nus}$	Flux 2–10 keV	Flux 15–55 keV	Lum. 2–10 keV	Lum. 15–55 keV
839/862	$1.64^{+0.02}_{-0.02}$	$0.0003^{+0.0001}_{-0.0001}$	$0.041^{+0.001}_{-0.001}$	$0.96^{+0.05}_{-0.05}$	$1.75^{+0.03}_{-0.02}\times10^{-12}$	$2.62^{+0.06}_{-0.10}\times10^{-12}$	$3.16^{+0.23}_{-0.14}\times10^{42}$	$5.01^{+0.24}_{-0.33}\times10^{42}$

Note. χ^2/dof: χ^2 divided by degrees of freedom. Γ: Power-law photon index. $N_{H,l.o.s.}$: line-of-sight torus hydrogen column density, in units of 10^{24} cm^2. norm: the main power-law normalization (in units of photons cm^2 s^1 keV^1 $\times$ 10^4), measured at 1 keV. $c_{\rm nus}$: The cross-normalization constant between the XMM and NuSTAR data. $F_{\rm 2-10\ keV}$: Observed flux in the 2–10 keV band with units of erg cm^{-2} s^{-1}. $F_{\rm 15-55\ keV}$: Observed flux in the 15–55 keV band with units of erg cm^{-2} s^{-1}. $L_{\rm 2-10\ keV}$: Intrinsic luminosity in the 2–10 keV band with units of erg s^{-1}. $L_{\rm 15-55\ keV}$: Intrinsic luminosity in the 15–55 keV band with units of erg s^{-1}.

typically encountered. Additionally, the true counterpart, 2MASX J04075215−6116126, was in the gap of the detector FPMB. For these reasons, this exposure could not provide valid scientific results and thus was not included in the analysis presented below.

3. X-Ray Spectral Analysis

Spectral fitting was conducted with `XSPEC` v. 12.11.1 (Arnaud 1996). The Galactic absorption in the direction of each source was calculated using the Heasoft tool `nh` (Kalberla et al. 2005). `clumin`[7] in `xspec` was used to calculate the intrinsic luminosity of each source in the 2–10 keV and 15–55 keV bands. Tables 2–5 list the results of the 0.6−78 keV spectral fitting. We note that each model implemented begins with a *constant*$_1$ that accounts for flux variations between the NuSTAR and XMM-Newton observations. In this section, we introduce the physically motivated models we used to fit the source spectra in Section 3.1, and the fitting results in Section 3.2.

3.1. Models Implemented

3.1.1. `MYTorus`

The first model applied in our analysis is `MYTorus` (Murphy & Yaqoob 2009). `MYTorus` assumes a torus of uniform absorbing material with circular cross section and an opening angle fixed to 60°, i.e., the covering factor = 0.50.

The model is composed of three different components: an absorbed line-of-sight continuum (MYTZ), a Compton-scattered continuum (MYTS), and a fluorescent line emission (MYTL). These three components are linked together with the same normalization, absorbing column density (the equatorial column density of the torus, $N_{\rm H,eq}$), and inclination angle θ_i. The inclination angle is measured from the axis of the torus, i.e., $\theta_i = 0°$ represents a face-on view and $\theta_i = 90°$ is an edge-on view. One can obtain the line-of-sight column density from the equatorial column density using

$$N_{\rm H,los} = N_{\rm H,eq} \times (1 - 4 \times \cos(\theta_i)^2)^{1/2}. \quad (1)$$

The average torus column density is not a separate parameter as the model treats it as equal to the line-of-sight column density. However, it can be determined in certain configurations.

The line-of-sight continuum, also called the zeroth-order continuum, is the intrinsic X-ray emission from the AGN observed after absorption from the torus along our line of sight. The Compton-scattered continuum is composed of the photons that interact with the dust and gas surrounding the SMBH and scatter into the observer line of sight. The final component includes the most significant fluorescent lines, i.e., the Fe Kα and Fe Kβ, at 6.4 and 7.06 keV, respectively. Both the reflected and fluorescent components are weighted by multiplicative constants, A_S and A_L, respectively, which can account for differences in the geometry and time delays between the three components. Additionally, we include an additional component, f_s, to fit the fraction of intrinsic emission that escapes the torus instead of becoming absorbed. Lastly, our model includes `mekal` to account for the emission below 3 keV caused by diffuse hot gas. `MYTorus` can be used in either the *coupled* or *decoupled* configuration (see Section 3.1.2). The model in `XSPEC` notation is as follows:

$$\begin{aligned}\text{ModelA} = {} & \text{constant}_1 * \text{phabs} * (\text{MYTZ}* \\ & \text{zpowerlw} + A_S * \text{MYTS} + A_L * \text{MYTL} \\ & + f_s * \text{zpowerlw} + \text{mekal}).\end{aligned} \quad (2)$$

In this work, we only present results using the decoupled configuration as `MYTorus` coupled has been shown to yield statistically worse fits and provides less information about the obscuring material average properties (see, e.g., Torres-Albà et al. 2021).

3.1.2. `MYTorus` in Decoupled Configuration

Unlike the coupled configuration, the `MYTorus` decoupled configuration (Yaqoob 2012) allows for the separate measurement of the line-of-sight column density, $N_{H,l.o.s.}$, and the average torus column density, $N_{\rm H,avg}$, thus mimicking a clumpy torus distribution. In this arrangement, the line-of-sight continuum has a fixed inclination angle of $\theta_{i,Z} = 90°$. The reflected and fluorescent line components can have their inclination angles fixed to both $\theta_{i,S} = 90°$ and $\theta_{i,S} = 0°$, representing an edge-on or face-on scenario, respectively. Additionally, their column densities are tied together to the average torus column density $N_{\rm H,avg}$.

3.1.3. *BORUS02*

The next physically motivated model utilized in this work is `borus02` (Baloković et al. 2018). Like `MYTorus`, `borus02` assumes a uniform obscuring material; however, the opening angle is not fixed. Thus, the covering factor c_f is a free parameter ($c_f \in$ [0.1,1]). The model only contains a reflection component, which includes both the reflection continuum and fluorescent lines. Therefore, we manually add the absorbed intrinsic continuum multiplied by a line-of-sight absorbing component, `zphabs` × `cabs`. `borus02` is implemented in

[7] https://heasarc.gsfc.nasa.gov/xanadu/xspec/manual/node285.html

Table 3
2MASX J04075215−6116126 NuSTAR-XMM-Newton

Model	MYTorus (Decoupled Face-on)	MYTorus (Decoupled Edge-on)	borus02	borus02 $\Gamma = 1.80$	UXClumpy
χ^2/dof	115/116	126/116	110/114	112/115	121/115
kT	$0.23^{+0.08}_{-0.08}$	$0.23^{+0.08}_{-0.08}$	$0.25^{+0.09}_{-0.07}$	$0.23^{+0.09}_{-0.09}$	$0.24^{+0.16}_{-0.13}$
Γ	$1.48^{+0.22}_{-u}$	$1.47^{+0.18}_{-u}$	$1.49^{+0.36}_{-u}$	1.80^{*}	$1.73^{+0.25}_{-0.13}$
norm 10^{-2}	$0.01^{+0.01}_{-0.01}$	$0.02^{+0.01}_{-0.01}$	$0.01^{+0.02}_{-0.01}$	$0.03^{+0.01}_{-0.01}$	$0.03^{+0.27}_{-0.01}$
$c_{f,Tor}$	…	…	$0.60^{-}_{-0.33}$	$0.54^{+0.37}_{-0.24}$	…
CTKcover	…	…	…	…	0^{*}
Tor σ	…	…	…	…	$28.2^{+u}_{-18.2}$
$\cos(\theta_{\rm obs})$	…	…	$0.85^{+u}_{-0.38}$	$0.75^{+u}_{-0.21}$	1.00^{+u}_{-u}
$N_{H,l.o.s.}$	$0.31^{+0.05}_{-0.03}$	$0.31^{+0.06}_{-0.04}$	$0.30^{+0.08}_{-0.03}$	$0.36^{+0.06}_{-0.05}$	$0.33^{+0.08}_{-0.04}$
$N_{\rm H,avg}$	$0.80^{+0.51}_{-0.41}$	$0.40^{+0.44}_{-0.22}$	$1.20^{+0.71}_{-0.76}$	$5.75^{+u}_{-4.49}$	…
f_s 10^{-2}	$3.56^{+1.10}_{-1.40}$	$3.43^{+1.00}_{-1.10}$	$3.61^{+0.80}_{-2.30}$	$1.89^{+0.69}_{-0.44}$	$8.24^{+13.0}_{-u}$
$c_{\rm nus}$	$1.45^{+0.16}_{-0.14}$	$1.44^{+0.17}_{-0.16}$	$1.50^{+0.17}_{-0.14}$	$1.57^{+0.15}_{-0.16}$	$1.55^{+0.16}_{-0.16}$
$F_{2-10\ \rm keV}$	$2.60^{+0.42}_{-1.06} \times 10^{-13}$	$2.57^{+0.46}_{-1.12} \times 10^{-13}$	$2.56^{+0.39}_{-1.11} \times 10^{-13}$	$2.55^{+0.12}_{-0.53} \times 10^{-13}$	$2.58^{+0.23}_{-2.89} \times 10^{-13}$
$F_{15-55\ \rm keV}$	$2.23^{+0.43}_{-0.74} \times 10^{-12}$	$2.33^{+0.39}_{-0.79} \times 10^{-12}$	$2.28^{+0.45}_{-0.81} \times 10^{-12}$	$2.24^{+0.15}_{-0.93} \times 10^{-12}$	$2.17^{+0.53}_{-2.63} \times 10^{-12}$
$L_{2-10\ \rm keV}$	$7.75^{+1.72}_{-3.49} \times 10^{41}$	$7.55^{+9.05}_{-2.00} \times 10^{41}$	$8.28^{+1.25}_{-0.69} \times 10^{41}$	$8.32^{+1.01}_{-0.91} \times 10^{41}$	$9.71^{+92.29}_{-2.93} \times 10^{41}$
$L_{15-55\ \rm keV}$	$2.31^{+0.51}_{-1.04} \times 10^{42}$	$2.67^{+3.21}_{-0.71} \times 10^{42}$	$1.00^{+0.10}_{-0.88} \times 10^{42}$	$1.86^{+0.14}_{-0.17} \times 10^{42}$	$1.96^{+18.54}_{-0.59} \times 10^{42}$

Note. Same as Table 2. Additional parameters: kT: `mekal` model temperature in units of keV. $c_{f,Tor}$: Covering factor of the torus. CTKcover: covering factor of the inner ring of clouds, computed with `UXClumpy`. Tor σ: cloud dispersion factor, computed with `UXClumpy`. $\cos(\theta_{\rm obs})$: cosine of the inclination angle. $N_{\rm H,avg}$: average torus hydrogen column density, in units of 10^{24} cm^2. f_s: fraction of scattered continuum.

`XSPEC` as follows:

$$\begin{aligned}\text{ModelB} = {} & \text{constant}_1 * \textit{phabs} * \\ & (\textit{borus02} + \textit{zphabs} * \text{cabs} * \textit{zpowerlw} \\ & + f_s * \textit{zpowerlaw}).\end{aligned} \quad (3)$$

Similarly to the decoupled configuration of `MYTorus`, `borus02` is capable of measuring both the line-of-sight and average torus column density. However, unlike `MYTorus` decoupled, `borus02` can constrain the observing angle in the range $\cos(\theta_{\rm inc}) = 0.05$–$0.9$.

`borus02` also includes a high-energy cutoff, which we freeze to 500 keV. We note that recent works find a lower average cutoff energy (∼200–300 keV; Ricci et al. 2017; Ananna et al. 2020; Baloković et al. 2021). However, the NuSTAR data for our sources correspond to <80 keV in the source rest frame; thus this change in high-energy cutoff would not affect our results.

3.1.4. UXClumpy

Unlike `borus02` and `MYTorus`, `UXClumpy` (Buchner et al. 2019) does not assume a uniform torus. Instead, `UXClumpy` is a physically motivated model that reproduces the data by simulating different cloud sizes and distributions. `UXClumpy` utilizes a Monte Carlo X-ray radiative transfer code, XARS, to compute the X-ray spectra of obscured AGN. The model is implemented in `XSPEC` as follows:

$$\begin{aligned}\text{ModelC} = {} & \text{constant}_1 * \text{phabs}* \\ & (\text{uxcl\_cutoff.fits}+ \\ & f_s * \text{uxcl\_cutoff\_omni.fits}).\end{aligned} \quad (4)$$

The first table accounts for the transmitted and reflection components, including fluorescent lines. `UXClumpy` produces the reflection component through the cloud distribution it generates. However, for some sources that are reflection dominated, a Compton-thick reflector near the corona can be added. This can be thought of as an inner wall that blocks the line of sight to the corona while also reflecting its emission. The second table reproduces the intrinsic continuum that leaks through the clumps of the torus.

`UXClumpy` differs from `borus02` in that it does not include a parameter to measure the average torus column density. However, it measures other torus parameters such as the inclination angle (with a slightly larger range than `borus02`; $\cos(\theta_{\rm inc}) = 0$–$1.00$), the dispersion of the cloud distribution `TORsigma` (σ ranges from 6 to 90°), and the covering factor of the inner reflector `CTKcover` (C ranges from 0 to 0.6).

3.2. Fitting Results

The spectra and resulting best-fit parameters can be found in Figures 1–4 and Tables 2–5, respectively. We note that the spectra of every source were fit starting from 0.6 keV, as this is the minimum allowed energy in `MYTorus`. We kept the same value in `borus02` and `UXClumpy` for consistency. Additionally, we left the NuSTAR cross-normalization constant $c_{\rm nus}$ free to vary in all models as even quasi-simultaneous XMM-Newton and NuSTAR observations can differ in the measured flux by up to 10% (see Table 5; Madsen et al. 2017).

3.2.1. 2MASX J02051994−0233055

Unlike the initial fits of 2MASX J02051994−0233055 in S22, which suggested it was a CT-AGN with line-of-sight column density $\sim 10^{25}$ cm^{-2}, the NuSTAR and XMM-Newton data are consistent with a power law. Therefore, we fit the data as such:

$$\textit{ModelD} = \textit{constant}_1 * \textit{phabs} * (\textit{zphabs} * \textit{zpowerlw}). \quad (5)$$

The results of this fit are presented in Table 2 and the spectra in Figure 1. The best-fit result for the line-of-sight column density is on the order of 10^{20} cm^{-2}, consistent with an

Table 4
ESO 362−8 NuSTAR -XMM-Newton

Model	MYTorus (Decoupled Face-on)	MYTorus (Decoupled Edge-on)	Borus02	Borus02 Two Γ	UXClumpy
χ^2/dof	71/82	72/82	80/81	71/80	68/80
kT	$0.66^{+0.10}_{-0.08}$	$0.66^{+0.11}_{-0.09}$	$0.62^{+0.06}_{-0.07}$	$0.65^{+0.07}_{-0.08}$	$0.77^{+0.08}_{-0.08}$
Γ	$1.90^{+0.17}_{-0.22}$	$1.41^{+0.08}_{-u}$	$2.6^{+u}_{-0.31}$	$1.80^{+0.44}_{-0.22}$	$1.68^{+0.13}_{-0.15}$
norm 10^{-2}	$0.14^{+0.03}_{-0.05}$	$0.05^{+0.01}_{-0.02}$	$2.14^{+0.60}_{-0.10}$	$0.09^{+1.81}_{-0.08}$	$0.29^{+1.54}_{-0.19}$
$c_{f,Tor}$	…	…	$0.90^{+0.08}_{-0.02}$	$0.91^{+0.08}_{-0.16}$	…
CTKcover	…	…	…	…	$0.31^{+u}_{-0.11}$
Tor σ	…	…	…	…	$14.0^{+u}_{-4.7}$
$\cos(\theta_{obs})$	…	…	$0.85^{+0.04}_{-0.08}$	$0.89^{+u}_{-0.09}$	1.00^{+u}_{-u}
$N_{H,l.o.s.}$	$2.78^{+u}_{-0.65}$	$2.18^{+0.21}_{-0.30}$	$3.96^{+u}_{-1.30}$	$2.57^{+1.40}_{-0.80}$	$3.93^{+u}_{-1.41}$
$N_{H,avg}$	$9.91^{+u}_{-5.66}$	$0.15^{+0.11}_{-0.04}$	$10^{+0.15}_{-4.75}$	$31.62^{+u}_{-11.11}$	…
f_s 10^{-2}	$0.90^{+0.80}_{-0.30}$	$2.60^{+1.00}_{-0.60}$	$0.05^{+0.01}_{-0.02}$	$1.40^{+3.60}_{-1.30}$	$1.20^{+5.50}_{-1.30}$
Γ #2	$3.03^{+0.35}_{-0.41}$	$2.94^{+0.32}_{-0.37}$	…	$2.92^{+0.38}_{-0.55}$	$3.00^{+u}_{-0.26}$
c_{nus}	$1.07^{+0.29}_{-0.20}$	$1.12^{+0.30}_{-0.19}$	$1.14^{+0.30}_{-0.25}$	$1.10^{+0.25}_{-0.23}$	$1.07^{+0.26}_{-0.21}$
$F_{2-10\ keV}$	$9.79^{+0.77}_{-2.54} \times 10^{-14}$	$1.04^{+3.87}_{-4.23} \times 10^{-13}$	$9.39^{+1.67}_{-5.02} \times 10^{-14}$	$1.00^{+3.12}_{-5.63} \times 10^{-13}$	$1.02^{+2.46}_{-5.32} \times 10^{-13}$
$F_{15-55\ keV}$	$2.19^{+1.01}_{-0.71} \times 10^{-12}$	$2.04^{+1.81}_{-0.99} \times 10^{-12}$	$1.73^{+0.78}_{-1.23} \times 10^{-12}$	$2.17^{+3.87}_{-3.83} \times 10^{-12}$	$2.19^{+3.45}_{-4.23} \times 10^{-12}$
$L_{2-10\ keV}$	$2.06^{+0.41}_{-0.75} \times 10^{42}$	$1.71^{+0.22}_{-0.74} \times 10^{42}$	$4.07^{+11.78}_{-} \times 10^{43}$	$2.82^{14.96}_{-} \times 10^{43}$	$5.43^{+31.67}_{-3.54} \times 10^{42}$
$L_{15-55\ keV}$	$2.34^{+0.47}_{-0.85} \times 10^{42}$	$4.91^{+0.65}_{-2.13} \times 10^{42}$	$2.51^{+2.06}_{-2.01} \times 10^{42}$	$1.20^{+0.35}_{-0.37} \times 10^{43}$	$1.05^{+5.64}_{-0.69} \times 10^{43}$

Note. Same as Table 3.

Table 5
IC 2227 NuSTAR-XMM-Newton

Model	MYTorus (Decoupled Face-on)	MYTorus (Decoupled Edge-on)	borus02	UXClumpy
χ^2/dof	165/140	180/140	165/138	172/138
kT	$0.63^{+0.06}_{-0.07}$	$0.62^{+0.06}_{-0.07}$	$0.63^{+0.06}_{-0.06}$	$0.75^{+0.07}_{-0.09}$
Γ	$1.86^{+0.20}_{-0.14}$	$1.75^{+0.23}_{-0.22}$	$1.87^{+0.12}_{-0.11}$	$1.95^{+0.19}_{-0.04}$
norm 10^{-2}	$0.09^{+0.09}_{-0.03}$	$0.07^{+0.09}_{-0.04}$	$0.09^{+0.05}_{-0.03}$	$0.13^{+0.01}_{-0.06}$
$c_{f,Tor}$	…	…	$0.80^{+0.07}_{-0.11}$	…
CTKcover	…	…	…	$0.60^{-}_{-0.11}$
Tor σ	…	…	…	$16.1^{+57.2}_{-12.6}$
$\cos(\theta_{obs})$	…	…	$0.78^{+0.12}_{-0.02}$	$1.00^{-}_{-0.59}$
$N_{H,l.o.s.}$	$0.60^{+0.11}_{-0.07}$	$0.58^{+0.08}_{-0.08}$	$0.64^{+0.05}_{-0.06}$	$0.63^{+0.10}_{-0.04}$
$N_{H,avg}$	$6.06^{-}_{-2.84}$	$1.37^{+1.96}_{-1.24}$	$31.62^{-}_{-26.00}$	…
f_s 10^{-2}	$0.90^{+0.50}_{-0.40}$	$1.10^{+1.10}_{-0.50}$	$0.90^{+0.60}_{-0.10}$	$3.20^{+3.00}_{-1.00}$
c_{nus}	$1.03^{+0.11}_{-0.10}$	$0.99^{+0.11}_{-0.10}$	$1.03^{+0.12}_{-0.06}$	$1.02^{+0.11}_{-0.11}$
$F_{2-10\ keV}$	$3.36^{+0.51}_{-0.87} \times 10^{-13}$	$3.45^{+0.39}_{-0.72} \times 10^{-13}$	$3.37^{+0.43}_{-1.09} \times 10^{-13}$	$3.40^{+0.27}_{-1.64} \times 10^{-13}$
$F_{15-55\ keV}$	$3.00^{+0.98}_{-1.60} \times 10^{-12}$	$2.72^{+0.52}_{-0.77} \times 10^{-12}$	$2.93^{+0.23}_{-1.32} \times 10^{-12}$	$2.74^{+0.88}_{-1.46} \times 10^{-12}$
$L_{2-10\ keV}$	$5.60^{+6.10}_{-1.70} \times 10^{42}$	$5.74^{+6.76}_{-3.40} \times 10^{42}$	$6.31^{+2.81}_{-0.94} \times 10^{42}$	$6.81^{+0.66}_{-3.07} \times 10^{42}$
$L_{15-55\ keV}$	$6.58^{+7.22}_{-1.99} \times 10^{42}$	$7.92^{+9.28}_{-4.69} \times 10^{42}$	$2.95^{+1.62}_{-0.95} \times 10^{42}$	$8.77^{+0.67}_{-4.06} \times 10^{42}$

Note. Same as Table 3.

unobscured AGN. Moreover, adding a reflection component does not statistically improve the fit. We will further discuss this significant discrepancy in Section 4.1.

3.2.2. 2MASX J04075215−6116126

The best-fit results in Table 3 show relatively consistent values between the different models. For example, all models yield a line-of-sight column density $\approx 0.30 \times 10^{24}$ cm^{-2}. Furthermore, all models agree that the source is observed through a less dense portion of the torus as the average column density has a larger value, even entering into the Compton-thick regime in the `borus02` best-fit results. Additionally, all models yield a photon index $\Gamma \sim 1.48$, a best-fit value somehow harder than it is commonly measured in AGN. To test the validity of this result, we froze the photon index to 1.8 and refit yielding largely similar results and near-indistinguishable fit statistics (a similar method was originally established in Nandra & Pounds 1994). As a consequence, we are unable to say which photon index is a better physical representation of this source. This is consistent with the large uncertainties measured.

Despite these observations taking place only 5 days apart, we find significant flux variation between NuSTAR and XMM-Newton with a best-fit NuSTAR cross-normalization constant $\approx$1.45. To verify this variation, we included Chandra data from 2018 (ObsID: 20440, exposure: 10.4 ks) and Swift-XRT data from 2018 (ObsID: 00094011001, exposure 2.3 ks) and 2021 (ObsID: 00089208002, exposure 2.1 ks). The two 2018 observations had a cross-normalization constant greater than 3 and the 2021 XRT observation had a constant $\approx$2. Furthermore, we tested if these variations could instead be coming from a column density fluctuation rather than intrinsic luminosity. When we left all the cross-normalization constants fixed to one and decoupled the column density of each observation, we found all observations yield a consistent line-of-sight $N_{H,l.o.s.}$ value $\approx 0.30 \times 10^{24}$ cm^{-2}. Therefore, we confirm that 2MASX J04075215−6116126 experienced a nearly 50% flux variation in just 5 days time and significant variation over 2 yr.

3.2.3. ESO 362−8

The initial fits of ESO 362−8 featured a very soft photon index ($\Gamma = 2.6$ in `borus02`), which is atypical of AGN, whose average value lies around ∼1.6–1.8 (Ricci et al. 2017). This

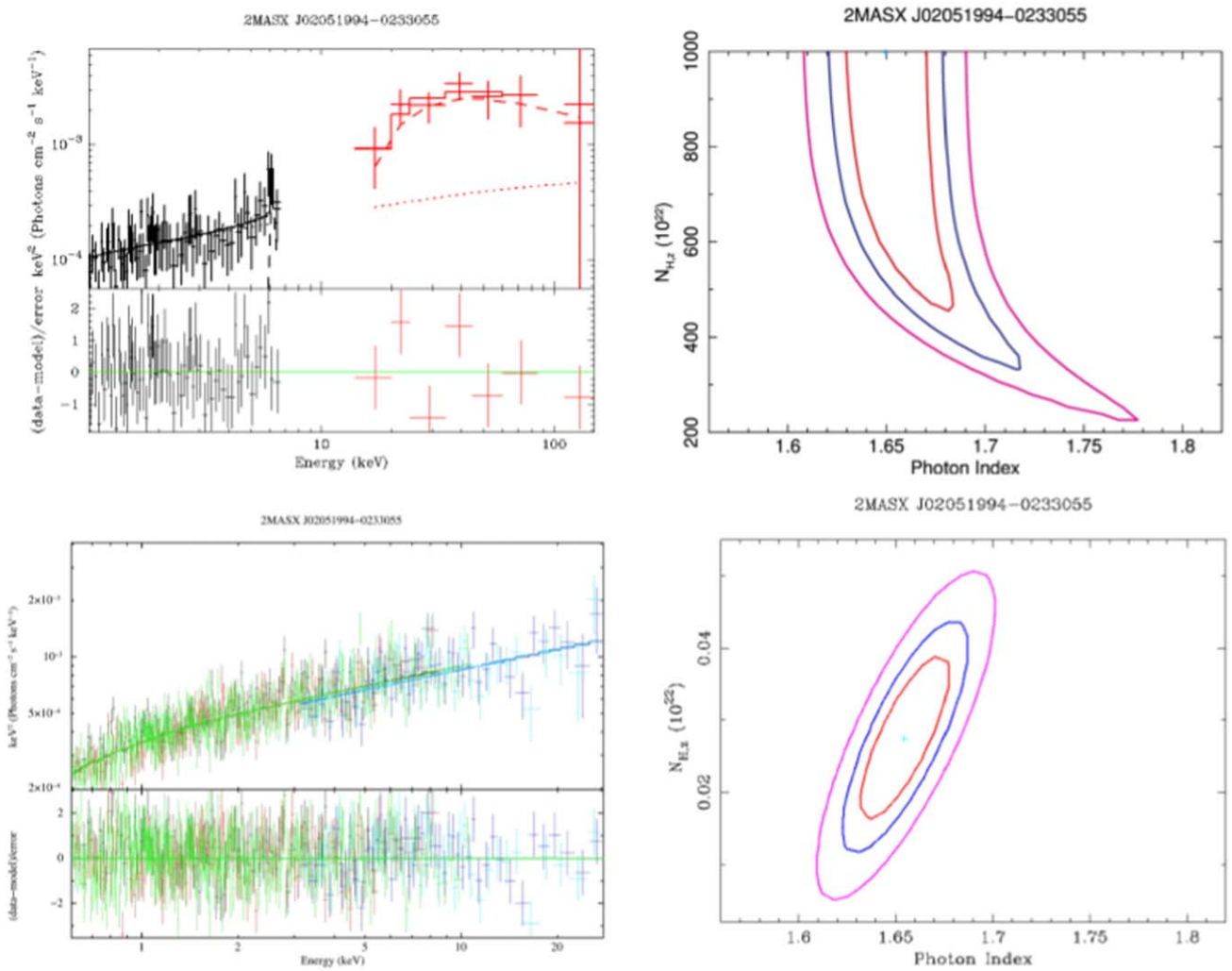

Figure 1. Top: the `borus02` fit of the Chandra-BAT data presented in S22 with the contours of $N_{H,l.o.s.}$ ($\times 10^{22}$ cm^{-2}) vs. photon index. The contours represent the 68%, 90%, and 99% confidence levels. Bottom: the NuSTAR−XMM-Newton data fit with a power law alongside its contour of the same parameters.

might be caused by an unusual excess in soft emission. To account for this, we first added a second `mekal` component. However, this only reduced the photon index to 2.4. Our next test decoupled the scattering emission photon index from the intrinsic emission photon index (as used in Torres-Albà et al. 2018). This difference in photon index stems from the contribution of X-ray binaries in sources with significant star formation. NuSTAR has recently been used to properly model these luminous and ultraluminous infrared galaxies (Teng et al. 2015; Puccetti et al. 2016; Ricci et al. 2021; Yamada et al. 2021). We find this to be our most physically plausible representation of the data, as the main power law has values from 1.70 to 1.90, and the scattered power law accounts for the soft excess with values from 2.90 to 3.00.

All models do agree that ESO 362−8 is a bona fide CT-AGN, with line-of-sight $N_{\rm H,l.o.s.}$ ranging from 2 to 4×10^{24} cm^{-2}. This is the first, and only, confirmed CT-AGN in this paper. Most applicable models also agree that the torus is Compton thick with $N_{\rm H,avg} \sim 1 \times 10^{25}$ cm^{-2}; however, the `MYTorus` edge-on fit only has an $N_{\rm H,avg} = 1.5 \times 10^{23}$ cm^{-2}. This discrepancy may be caused by the fact that we are viewing the source nearly face-on (as supported by `borus02` and `UXClumpy`), while this model configuration tries to force the edge-on view. Finally, `borus02` and `UXClumpy` agree on the parameters constraining the torus, such as the near-face-on inclination angle (∼0.90–1.00) and a significant covering factor (0.90 for `borus02` and 0.31 for `UXClumpy`).

3.2.4. IC 2227

All models agree that IC 2227 is a Compton-thin AGN with line-of-sight $N_{\rm H,l.o.s.} \sim 0.6 \times 10^{24}$ cm^{-2}. They are also consistent with yielding a photon index around 1.8. Furthermore, the models agree that this source is reflection dominated due to its Compton-thick average torus $N_{\rm H,avg}$, ranging from 1.4 to 31×10^{24} cm^{-2}, and a large covering factor of 0.80 and 0.60 from `borus02` and `UXClumpy`, respectively.

4. Discussion

This work serves as the third step in our previously proven successful process (Zhao et al. 2019a, 2019b) of identifying and characterizing CT-AGN in the local universe. First, we used the selection criteria laid out in S22 to discover potentially obscured AGN and propose them to Chandra. Next, we analyze the Chandra snapshots along with Swift-BAT data to determine a preliminary line-of-sight column density value. Finally, we use these results to pick the best CT-AGN candidates and propose for joint NuSTAR−XMM-Newton observations, thus

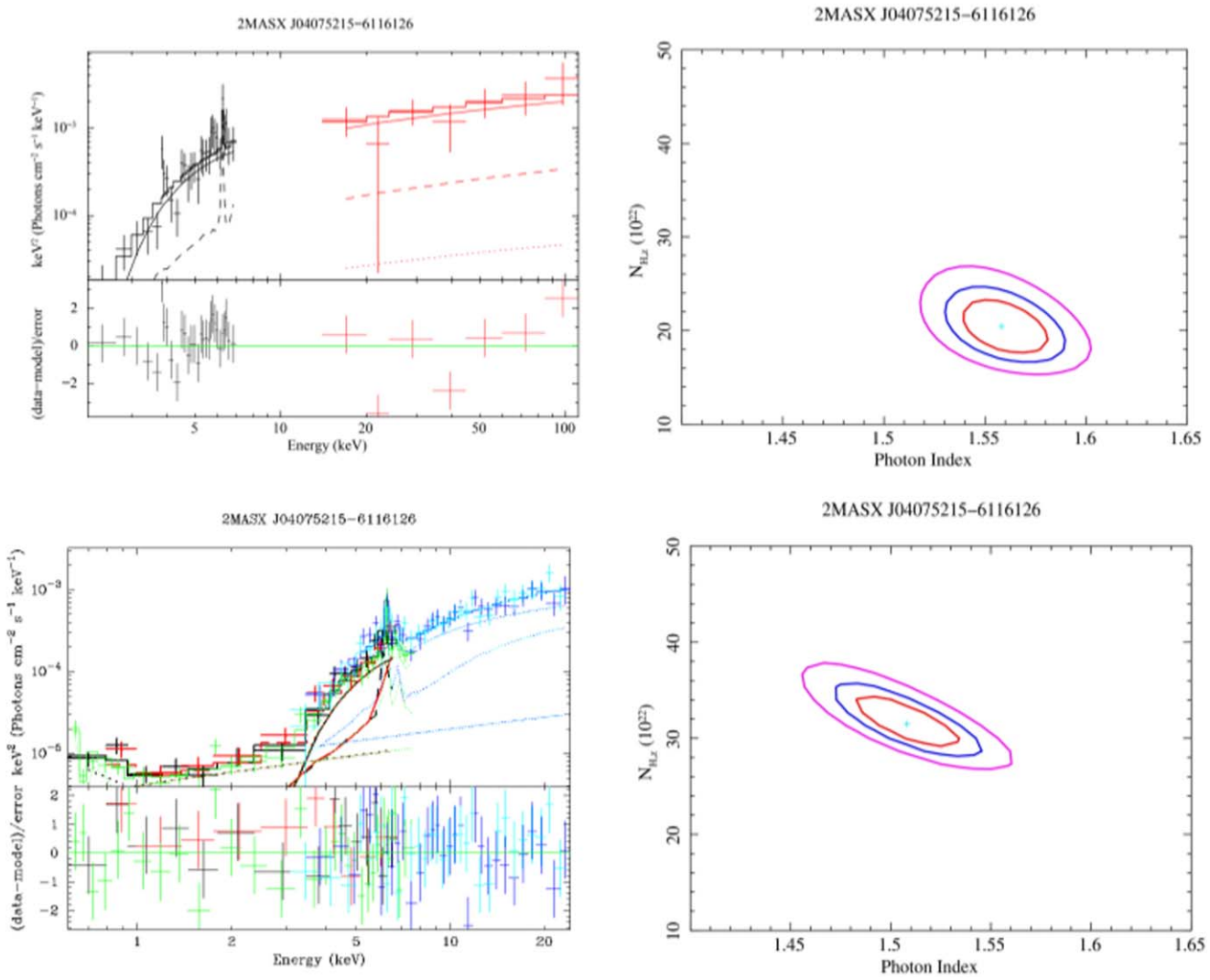

Figure 2. Top: the `borus02` fit for the Chandra-BAT data of 2MASX J04075215−6116126 presented in S22 with the contours of $N_{H,l.o.s.}$ ($\times 10^{22}$ cm^{-2}) vs. photon index. The contours represent the 68%, 90%, and 99% confidence levels. Bottom: the `borus02` fit of the NuSTAR−XMM-Newton data alongside its contour of the same parameters.

allowing us to confirm whether or not these candidates are Compton thick and to measure properties of the obscuring material, such as its average column density and covering factor.

4.1. Comparison with Previous Results

4.1.1. 2MASX J02051994−0233055

S22 listed 2MASX J02051994−0233055 as a Compton-thick candidate, finding a line-of-sight column density of 1×10^{25} cm^{-2}, but with large uncertainties (∼70%). The NuSTAR−*XMM* analysis discovered that 2MASX J02051994−0233055 is not a CT-AGN, in fact, it is an unobscured AGN. Our typical obscured-AGN models described in Section 3.1, which include significant contribution from a reprocessing component, were unable to satisfactorily fit the data. Instead, an absorbed power law was used and found a line-of-sight column density of 3×10^{20} cm^{-2} with smaller uncertainties (∼30%).

The Chandra−BAT analysis labeled this as a CT-AGN candidate likely due to the source being in an extremely low flux state during the Chandra observation. To confirm this variability, we plotted in Figure 5 the XMM-Newton (magenta, orange, and yellow) and NuSTAR (blue and cyan) data alongside the BAT (red), Chandra observation (from 2018 June, black), and Swift-XRT observation (from 2018 June, green). The XRT observation, taken during the same week as the Chandra observation, has a similar flux level (see Figure 6), confirming the variability. Even more interestingly, the BAT data (which are an average over 150 months) are at a higher flux level than even the NuSTAR and XMM data. This suggests that if the Chandra state has a flux 5× lower than the BAT data (in the 2–10 keV band), there could also have been a time when the source was in a flux state 5× higher than the BAT data.

We note that while some AGN have shown line-of-sight $N_{\rm H}$ variability (see, e.g., Risaliti et al. 2010; Markowitz et al. 2014; Laha et al. 2020; Pizzetti et al. 2022), no source has yet varied from a Compton-thick AGN state to an unobscured one. Therefore, it is much more likely that intrinsic luminosity variability is responsible for the change in spectral shape of 2MASX J02051994−0233055, as is supported statistically by our fits. This source marks the first time since beginning our search for CT-AGN that our selection criteria yielded an unobscured AGN. Such a result further highlights the

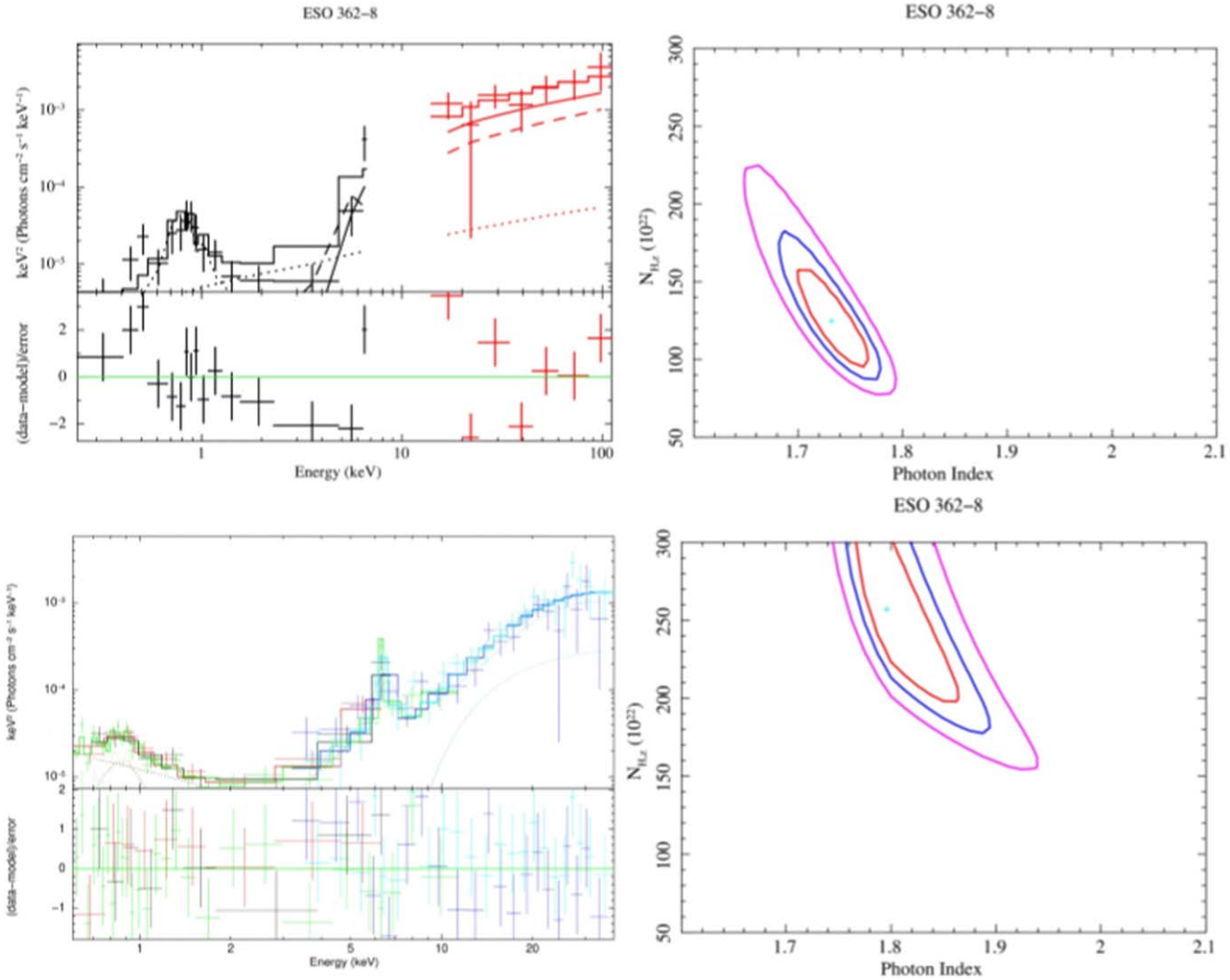

Figure 3. Top: the `borus02` fit for the archival XMM-BAT data of ESO 362−8 with the contours of $N_{H,l.o.s.}$ ($\times 10^{22}$ cm^{-2}) vs. photon index. The contours represent the 68%, 90%, and 99% confidence levels. Bottom: the `borus02` fit of the NuSTAR−XMM-Newton data alongside its contour of the same parameters.

importance of simultaneous NuSTAR and XMM-Newton observations in determining the column density of AGN.

4.1.2. 2MASX J04075215−6116126

The joint Chandra-Swift-BAT spectrum of 2MASX J04075215−6116126 was analyzed in S22 and found to be a Compton-thin candidate, with a line-of-sight column density of $2.10^{+0.04}_{-0.08} \times 10^{23}$ cm^{-2} (this is the `borus02` result; other models produced similar values). The NuSTAR−XMM-Newton analysis presented in this paper yielded similar results ($\sim 3 \times 10^{23}$ cm^{-2}), confirming this source to be a Compton-thin AGN. This work found the average torus column density to be larger than previously found, even entering the Compton-thick regime in the `borus02` results. However, this difference could be caused by the larger uncertainties from the Chandra−BAT fits (>140% uncertainties versus ∼80% uncertainties in this work).

4.1.3. ESO 362−8

Neither ESO 362−8 nor IC 2227 have previously published $N_{\rm H}$ values. Instead, we compare to the results found from fitting the archival data with BAT spectra. We note that at the time of the proposal, neither source had BAT spectra available to us. Instead, the archival data was jointly fit with BAT data from other sources that were newly discovered in the 150 month catalog (just as ESO 362−8 and IC 2227 were, and thus are expected to have very similar flux levels).

The 18 ks archival XMM-Newton observation of ESO 362−8 from 2006 February yielded a photon index of 1.73 and an $N_{\rm H,l.o.s.} = 1.25 \times 10^{24}$ cm^{-2}. The photon index is in good agreement with the simultaneous NuSTAR and XMM data, as most models yielded ∼1.8. The new results also confirmed this source as Compton thick, but with a larger $N_{\rm H,l.o.s.}$, $>2 \times 10^{24}$ cm^{-2} than that found in the archival data.

4.1.4. IC 2227

The 20 ks archival XRT data from 2008 May for IC 2227 produced a best-fit photon index of 1.81 and $N_{\rm H,l.o.s.} = 1.23 \times 10^{24}$ cm^{-2}. The NuSTAR and XMM-Newton data found a similar photon index, with most models around 1.85. However, the new data found IC 2227 to be Compton thin, not Compton thick as predicted by the XRT results. While the archival data are consistent with a Compton-thin scenario within 90% confidence (9×10^{23} cm^{-2}; see the blue line in Figure 4), it does not fall as low as the 6×10^{23} cm^{-2} value

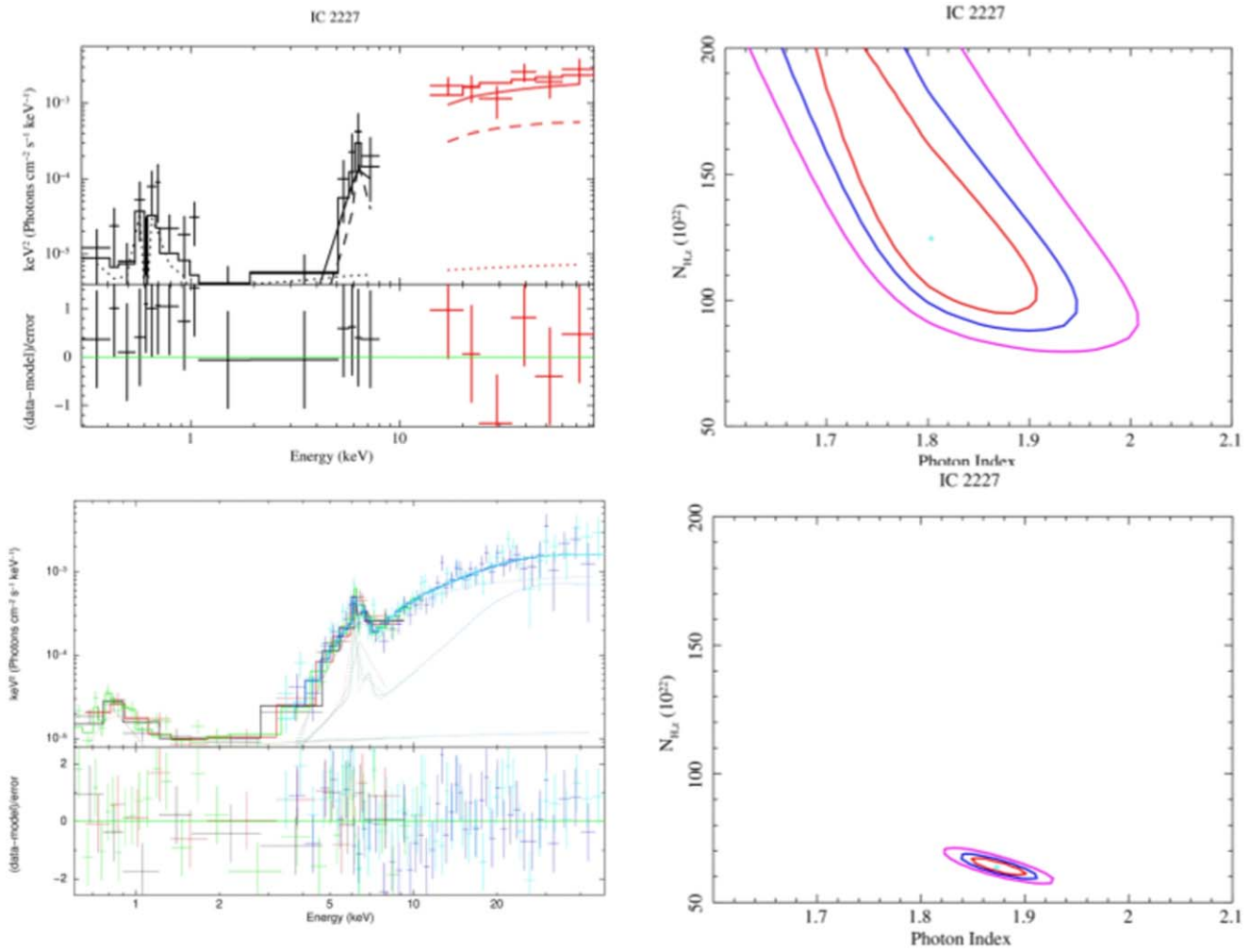

Figure 4. Top: the `borus02` fit for the archival XRT-BAT data of IC 2227 with the contour of $N_{H,l.o.s.}$ ($\times 10^{22}$ cm^{-2}) vs. photon index. The contours represent the 68%, 90%, and 99% confidence levels. Bottom: the `borus02` fit of the NuSTAR−XMM-Newton data alongside its contour of the same parameters.

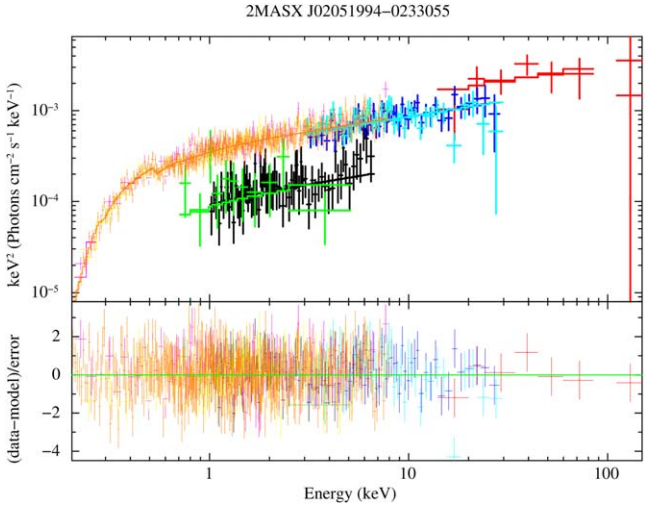

Figure 5. Data of 2MASX J02051994−0233055 from multiple instruments demonstrating the source's flux variability while maintaining a consistent photon index. The Chandra data is in black (taken in 2018); BAT (average spectrum obtained combining the data taken between 2005 and 2017) in red; XMM-Newton in orange, yellow, and magenta (2021); NuSTAR in blue and cyan (2021); Swift-XRT in green (2018).

found by the new data. There are at least two possible explanations to this discrepancy: (1) the XRT data were not of a high enough quality to accurately estimate the true $N_{\rm H,l.o.s.}$ of the source (Marchesi et al. 2018 found that XRT+BAT fits often overestimate $N_{\rm H,l.o.s.}$), or (2) IC 2227 experienced variability in its line-of-sight column density between the XRT observation in 2008–2009 and its NuSTAR and XMM-Newton observations in 2022. This source may be targeted again in the future to identify if there is true $N_{\rm H,l.o.s.}$ variability present.

4.2. Clemson-INAF CT-AGN Project

Using joint fits of soft X-ray and BAT data, Ricci et al. 2015 presented a list of CT-AGN candidates in the 70 month BAT catalog. 55 sources were listed, with 50 having $z \leqslant 0.05$. Adding sources from the Palermo 100 catalog (Cusumano et al. 2014), more recent works (Marchesi et al. 2017a, 2017b), and the four sources presented in this paper, brings this list up to 65 CT-AGN candidates with $z \leqslant 0.05$. Including this work, our group has now personally analyzed 52 of these sources, confirming 28 to be CT-AGN based on their simultaneous NuSTAR-XMM data. This is a roughly ∼50% success rate,

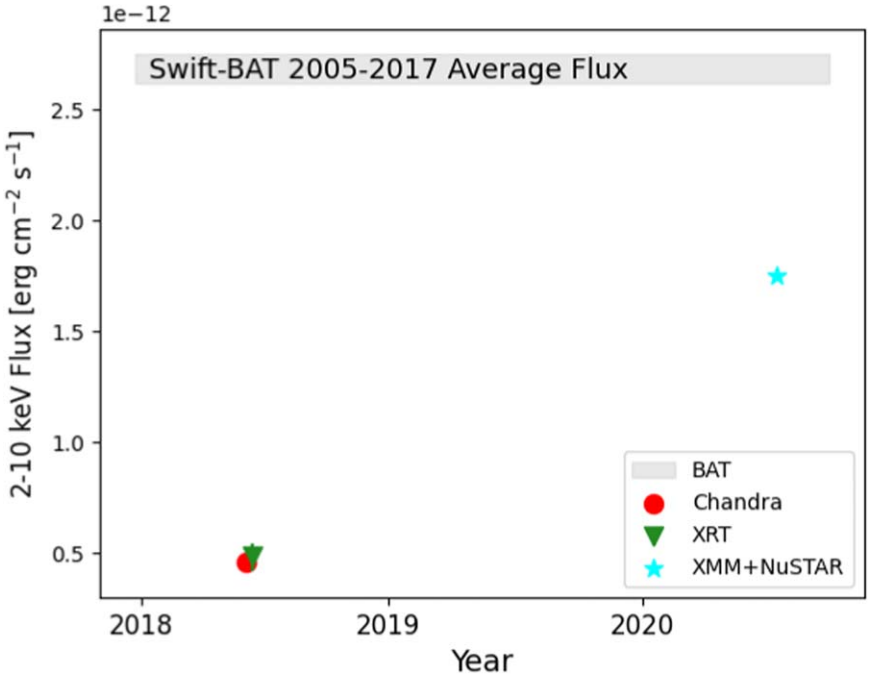

Figure 6. The 2–10 keV flux of 2MASX J02051994-0233055 as a function of time over the past 15 yr. The red circle and green triangle are the best-fitted fluxes from Chandra (2018 June 11 date) and XRT (2008 June 25) observations. The cyan star is the source flux obtained in July 2020 by NuSTAR and XMM-Newton. The gray filled region shows the 12 yr average flux from the Swift-BAT observations in 2005–2017, which is converted from its 14-195 keV flux to 2−10 keV flux. The light curve suggests that 2MASX J02051994-0233055 has experienced a more than 5 times flux variability in the last 15 yr due to the different accretion rates as analyzed in Section 4.1.1. Uncertainties on the fluxes are plotted but are too small to be visible.

highlighting the significance of NuSTAR for confirming sources as CT-AGN. In total, there have now been 35 CT-AGN discovered in the local Universe[8] (Torres-Albà et al. 2021).

4.3. Observational Evidence for Nonhomogeneity of the Obscuring Material

Figure 7 compares the line-of-sight column density with the average torus column density of CT-AGN candidates studied as a part of this project (see Marchesi et al. 2019; Torres-Albà et al. 2021; Traina et al. 2021; Zhao et al. 2021). The figure shows no visible trend between the two values, i.e., CT-AGN are no more likely to have Compton-thick tori compared to less-obscured AGN. This supports the idea that the material causing the X-ray obscuration is not a homogeneous structure. Instead, it is comprised of differing density clumps that revolve around the central engine, moving into and out of our line of sight. This can lead to different $N_{\rm H,l.o.s.}$ measurements when a source has multiepoch observations. This has been proven in recent works on sources such as NGC 7479 (Pizzetti et al. 2022), NGC 1358 (Marchesi et al. accepted), and in a sample of Compton-thin (Zhao et al. 2021) and Compton-thick (N. Torres-Albà 2022, in preparation) sources. The three obscured AGN in our sample[9] (i.e., excluding 2MASX J02051994−0233055) all lie away from the diagonal dashed line, thus further supporting this hypothesis. As already discussed, this difference is especially true with IC 2227, making it a potential candidate for future monitoring.

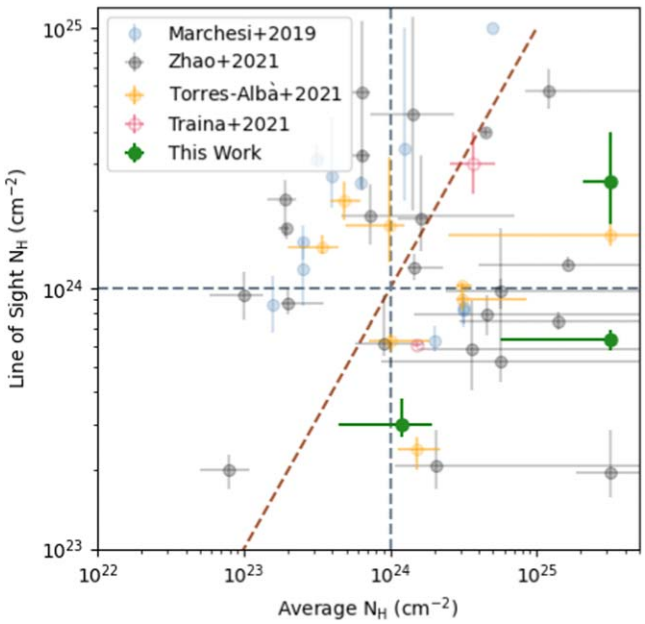

Figure 7. The `borus02` best-fit values of line-of-sight column density vs. the average column density of the AGN in this project. The three sources in this work are shown in green. 2MASX J02051994−0233055 is not included as it is unobscured, and thus, we are unable to provide an average torus column density measurement. The vertical and horizontal dashed lines represent the CT threshold, while the diagonal dashed line is the one-to-one relationship between $N_{\rm H,los}$ and $N_{\rm H,avg}$. Other sources are from Marchesi et al. (2019), Torres-Albà et al. (2021), Traina et al. (2021), and Zhao et al. (2021).

5. Conclusions

In this work, we have analyzed simultaneous NuSTAR and XMM-Newton data of four CT-AGN candidates with the physically motivated tori models `MYTorus`, `borus02`, and

[8] https://science.clemson.edu/ctagn/ctagn/

[9] Since 2MASX J02051994−0233055 is found to be unobscured, its reprocessed emission cannot be reliably measured. As a consequence, no measurement of the average torus column density can also be performed.

UXClumpy. None of the sources have had NuSTAR data published previously. We summarize our conclusions as follows:

1. Of the four sources analyzed, one, ESO 362−8, is confirmed to be a bona fide CT-AGN. This increases the sample of BAT-detected CT-AGN in the local universe ($z < 0.1$) to 35.
2. 2MASX J02051994-0233055 was determined to be a highly flux-variable, unobscured AGN. This is the first source studied using our criteria to select heavily obscured AGN that was instead discovered to be unobscured due to its strong flux variability. This highlights the importance of simultaneous soft and hard X-ray observations to accurately classify and characterize the heavily obscured AGN population.
3. 2MASX J04075215-6116126 displayed significant flux variation (∼50%) in only 5 days separating observations. Moreover, the flux varied by a factor of 3 when compared with observations taken 2 yr prior. It was confirmed that $N_{\rm H,los}$ remained constant during these periods, thus providing another example of an AGN with significant luminosity variation. Such sources can be studied to probe the relationship between the luminosity and the geometry of the obscuring (i.e., covering factor).
4. All three sources with $N_{\rm H,los} > 10^{23}\,{\rm cm}^{-2}$ show statistically significant differences in their line-of-sight and average torus column densities. This further supports that the structure of the obscuring material surrounding accreting SMBHs may be clumpy, rather than uniform.

R.S., N.T.A., A.P., and M.A. acknowledge NASA funding under contracts 80NSSC20K0045, 80NSSC19K0531, 80NSSC21K0016, and 80NSSC22K0005 and SAO funding under contracts GO0-21083X and G08-19083X. S.M. acknowledges funding from the the INAF "Progetti di Ricerca di Rilevante Interesse Nazionale" (PRIN), Bando 2019 (project: "Piercing through the clouds: a multiwavelength study of obscured accretion in nearby supermassive black holes").

ORCID iDs

R. Silver https://orcid.org/0000-0001-6564-0517
N. Torres-Albà https://orcid.org/0000-0003-3638-8943
S. Marchesi https://orcid.org/0000-0001-5544-0749
A. Pizzetti https://orcid.org/0000-0001-6412-2312
I. Cox https://orcid.org/0000-0003-2287-0325
M. Ajello https://orcid.org/0000-0002-6584-1703
A. Segreto https://orcid.org/0000-0001-7341-6603

References

Ajello, M., Greiner, J., Sato, G., et al. 2008, ApJ, 689, 666
Alexander, D. M., Bauer, F. E., Brandt, W. N., et al. 2003, AJ, 126, 539
Ananna, T. T., Treister, E., Megan Urry, C., et al. 2019, ApJ, 871, 240
Ananna, T. T., Treister, E., Urry, C. M., et al. 2020, ApJ, 889, 17
Arnaud, K. A. 1996, in ASP Conf. Ser., 101, Astronomical Data Analysis Software and Systems V, ed. G. H. Jacoby & J. Barnes (San Francisco, CA: ASP), 17
Baloković, M., Brightman, M., Harrison, F. A., et al. 2018, ApJ, 854, 42
Baloković, M., Cabral, S. E., Brenneman, L., & Urry, C. M. 2021, ApJ, 916, 90
Baloković, M., Comastri, A., Harrison, F. A., et al. 2014, ApJ, 794, 111
Barthelmy, S. D., Barbier, L. M., Cummings, J. R., et al. 2005, SSRv, 120, 143
Brandt, W. N., & Yang, G. 2021, arXiv:2111.01156
Buchner, J., Brightman, M., Nandra, K., Nikutta, R., & Bauer, F. E. 2019, A&A, 629, A16
Burlon, D., Ajello, M., Greiner, J., et al. 2011, ApJ, 728, 58
Comastri, A. 2004, in Supermassive Black Holes in the Distant Universe, ed. A. J. Barger (Dordrecht: Kluwer), 245
Cusumano, G., Segreto, A., La Parola, V., & Maselli, A. 2014, in Proc. Swift: 10 Years of Discovery (SWIFT) (Trieste: SISSA), 132
Della Ceca., R., Caccianiga, A., Severgnini, P., et al. 2008, A&A, 487, 119
Gilli., R., Comastri, A., & Hasinger, G. 2007, A&A, 463, 79
Harrison, F. A., Craig, W. W., Christensen, F. E., et al. 2013, ApJ, 770, 103
Jansen, F., Lumb, D., Altieri, B., et al. 2001, A&A, 365, L1
Kalberla, P. M. W., Burton, W. B., Hartmann, D., et al. 2005, A&A, 440, 775
Koss, M. J., Assef, R., Balokovic, M., et al. 2016, ApJ, 825, 85
Laha, S., Markowitz, A. G., Krumpe, M., et al. 2020, ApJ, 897, 66
Madsen, K. K., Beardmore, A. P., Forster, K., et al. 2017, AJ, 153, 2
Marchesi, S., Ajello, M., Comastri, A., et al. 2017a, ApJ, 836, 116
Marchesi, S., Ajello, M., Marcotulli, L., et al. 2018, ApJ, 854, 49
Marchesi, S., Ajello, M., Zhao, X., et al. 2019, ApJ, 882, 162
Marchesi, S., Tremblay, L., Ajello, M., et al. 2017b, ApJ, 848, 53
Markowitz, A. G., Krumpe, M., & Nikutta, R. 2014, MNRAS, 439, 1403
Murphy, K. D., & Yaqoob, T. 2009, MNRAS, 397, 1549
Nandra, K., & Pounds, K. A. 1994, MNRAS, 268, 405
Pizzetti, A., Torres-Alba, N., Marchesi, S., et al. 2022, ApJ, 936, 149
Puccetti, S., Comastri, A., Bauer, F. E., et al. 2016, A&A, 585, A157
Ricci, C., Privon, G. C., Pfeifle, R. W., et al. 2021, MNRAS, 506, 5935
Ricci, C., Trakhtenbrot, B., Koss, M. J., et al. 2017, ApJS, 233, 17
Ricci, C., Ueda, Y., Koss, M. J., et al. 2015, ApJ, 815, L13
Risaliti, G., Elvis, M., Bianchi, S., & Matt, G. 2010, MNRAS, 406, L20
Silver, R., Torres-Albà, N., Zhao, X., et al. 2022, ApJ, 932, 43
Teng, S. H., Rigby, J. R., Stern, D., et al. 2015, ApJ, 814, 56
Torres-Albà, N., Iwasawa, K., Díaz-Santos, T., et al. 2018, A&A, 620, A140
Torres-Albà, N., Marchesi, S., Zhao, X., et al. 2021, ApJ, 922, 252
Traina, A., Marchesi, S., Vignali, C., et al. 2021, ApJ, 922, 159
Treister, E., Urry, C. M., & Virani, S. 2009, ApJ, 696, 110
Ueda, Y., Akiyama, M., Hasinger, G., Miyaji, T., & Watson, M. G. 2014, ApJ, 786, 104
Ursini, F., Bassani, L., Panessa, F., et al. 2018, MNRAS, 474, 5684
Voges, W., Aschenbach, B., Boller, T., et al. 1999, A&A, 349, 389
Yamada, S., Ueda, Y., Tanimoto, A., et al. 2021, ApJS, 257, 61
Yaqoob, T. 2012, MNRAS, 423, 3360
Zhao, X., Marchesi, S., & Ajello, M. 2019a, ApJ, 871, 182
Zhao, X., Marchesi, S., Ajello, M., et al. 2019b, ApJ, 870, 60
Zhao, X., Marchesi, S., Ajello, M., et al. 2021, A&A, 650, A57